

# On the interactions between a propagating shock wave and evaporating water droplets

EP

Cite as: Phys. Fluids **32**, 123315 (2020); <https://doi.org/10.1063/5.0035968>

Submitted: 01 November 2020 . Accepted: 02 December 2020 . Published Online: 23 December 2020

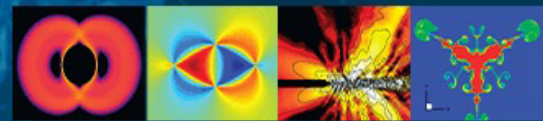
 Zhiwei Huang (黄志伟), and  Huangwei Zhang (张黄伟)

## COLLECTIONS

 This paper was selected as an Editor's Pick

[View Online](#)[Export Citation](#)[CrossMark](#)

Physics of Fluids  
**GALLERY OF COVERS**



# On the interactions between a propagating shock wave and evaporating water droplets

Cite as: Phys. Fluids 32, 123315 (2020); doi: 10.1063/5.0035968

Submitted: 1 November 2020 • Accepted: 2 December 2020 •

Published Online: 23 December 2020



View Online



Export Citation



CrossMark

Zhiwei Huang (黄志伟)  and Huangwei Zhang (张黄伟) <sup>a)</sup> 

## AFFILIATIONS

Department of Mechanical Engineering, National University of Singapore, 9 Engineering Drive 1, Singapore 117576, Republic of Singapore

<sup>a)</sup> Author to whom correspondence should be addressed: [huangwei.zhang@nus.edu.sg](mailto:huangwei.zhang@nus.edu.sg). Tel.: +65 6516 2557.

## ABSTRACT

One-dimensional numerical simulations based on the hybrid Eulerian–Lagrangian approach are performed to investigate the interactions between propagating shock waves and dispersed evaporating water droplets in two-phase gas–droplet flows. Two-way coupling for interphase exchanges of mass, momentum, and energy is adopted. A parametric study on shock attenuation, droplet evaporation, motion, and heating is conducted, through considering various initial droplet diameters ( $5\ \mu\text{m}$ – $20\ \mu\text{m}$ ), number densities ( $2.5 \times 10^{11}/\text{m}^3$ – $2 \times 10^{12}/\text{m}^3$ ), and incident shock Mach numbers (1.17–1.9). It is found that the leading shock may be attenuated to the sonic wave and even to the subsonic wave when the droplet volume fraction is large and/or the incident shock Mach number is low. Attenuation in both strength and propagation speed of the leading shock is mainly caused by momentum transfer to the droplets that interact at the shock front. Total pressure recovery is observed in the evaporation region, whereas pressure loss results from shock compression, droplet drag, and pressure gradient force behind the shock front. Recompression of the region between the leading shock and the two-phase contact surface is observed when the following compression wave is supersonic. After a critical point, this region gets stable in width and interphase exchanges in mass, momentum, and energy. However, the recompression phenomenon is sensitive to the droplet volume fraction and may vanish with high droplet loading. For an incident shock Mach number of 1.6, recompression only occurs when the initial droplet volume fraction is below  $3.28 \times 10^{-5}$ .

Published under license by AIP Publishing. <https://doi.org/10.1063/5.0035968>

## I. INTRODUCTION

The interactions between propagating shock waves and evaporating droplets are fundamental but challenging multi-phase problems. Studies on such topics have been performed for decades in different fields, e.g., aerospace propulsion,<sup>1–3</sup> internal combustion engine,<sup>4–6</sup> and shock tube.<sup>7–9</sup> Due to the simplicity in geometry and convenience for a parametric study, shock–droplet or shock–particle interactions have been extensively investigated in shock tube facilities. A series of shock tube experiments have been conducted to study the influence of a cloud of water droplets on the propagation of a planar shock wave.<sup>8</sup> Although wall pressure data have been recorded for further analysis on shock attenuation, details on droplet evaporation and movement as well as interphase interactions were not attainable due to the limitations of experimental measurement. The interactions of a shock wave and a single water droplet with inside vapor cavitation have been experimentally studied in a shock tube.<sup>9</sup> The evolutions of both the droplet and the vapor cavity have

been recorded with a high-speed imaging technique. However, the focus has been laid on the droplet deformation and cavity collapse. As in other shock tube experiments,<sup>10,11</sup> more detailed information is difficult to be measured due to the limitations of measurement techniques, e.g., evolutions of shock strength and Mach number, droplet volume fraction, response timescales, and interphase coupling. Therefore, the effects of shock waves on dispersed droplets and the interphase exchanges of mass, momentum, and energy are still not well understood in shocked two-phase flows.

A methodology for simulating two-phase flows considering two-way coupling has been developed to investigate the effect of droplet mass and heat transfer on one-dimensional (1D) shock waves.<sup>7</sup> However, the focus was on the shock attenuation, instead of detailed evolutions of droplet properties, e.g., diameter and temperature. Recently, the effect of shock waves on the dispersion characteristics of a particle cloud has been investigated both numerically and analytically.<sup>12</sup> A one-dimensional one-way coupling analytical study is conducted to estimate the cloud topology in the wake of a shock

wave. Moreover, a two-way formalism is developed, through further considering post-shock gas deceleration due to dispersed particles. However, evaporation, pressure gradient force (PGF), heat transfer, and gas viscosity are all neglected in the above work. The only coupling between the two phases is the particle momentum equation with drag force.

In this work, numerical studies are performed with a hybrid Eulerian–Lagrangian method to investigate the interactions between a propagating shock wave and evaporating water droplets. The two-way interphase coupling of mass, momentum, and energy is considered. To better describe the kinematic effects of a shock wave on dispersed droplets, the PGF is considered in our model, besides the drag force. The objectives are two-fold. First, the interactions between dispersed evaporating droplets and shock waves are investigated under a range of operating conditions. Shock attenuation in both strength and Mach number, droplet temperature, velocity, and diameter variations are studied. This differs from the previous work, e.g., in Refs. 7–11, which are mainly focused on shock attenuation or droplet breakup. Second, the evolutions of the two-phase interactions are discussed in detail, which allows detailed demonstrations of the unsteady process with novel two-phase flow phenomena, e.g., gas recompression in the droplet-laden area. The rest of this paper is organized as follows. Numerical approaches, including governing equations and numerical schemes, are described in Sec. II. Physical models and mesh sensitivity analysis are given in Secs. III and IV, respectively. The results and discussion are presented in Sec. V, and the conclusions are drawn in Sec. VI.

## II. GOVERNING EQUATION AND NUMERICAL METHOD

### A. Governing equations for gas phase

The governing equations for compressible multi-component flows include the conservation laws of mass, momentum, energy, and species mass fraction.<sup>13</sup> They read as

$$\frac{\partial \rho_g}{\partial t} + \frac{\partial}{\partial x_i} (\rho_g u_{g,i}) = S_m, \quad (1)$$

$$\frac{\partial}{\partial t} (\rho_g u_{g,i}) + \frac{\partial}{\partial x_j} (\rho_g u_{g,j} u_{g,i} + p_g \delta_{ij} - \tau_{ij}) = S_{M,i}, \quad (2)$$

$$\frac{\partial}{\partial t} (\rho_g E_g) + \frac{\partial}{\partial x_i} (\rho_g E_g u_{g,i} - q_i - \tau_{ij} u_{g,i} + p u_{g,i}) = S_e, \quad (3)$$

$$\frac{\partial}{\partial t} (\rho_g Y_m) + \frac{\partial}{\partial x_i} (\rho_g Y_m u_{g,i}) - \frac{\partial}{\partial x_i} \left( \rho_g D_g \frac{\partial Y_m}{\partial x_i} \right) = S_{Y_m}, \quad (4)$$

respectively, where  $t$  is the time and  $x$  is the spatial coordinate.  $\rho_g$  is the gas density,  $u_{g,i}$  is the gas velocity component,  $p_g$  is the gas pressure,  $\delta_{ij}$  is the Kronecker delta function, and  $\tau_{ij}$  is the viscous stress tensor.  $E_g$  is the total energy, which is calculated as  $E_g = e_{s,g} + \sum_{i=1}^3 u_{g,i}^2$ , with  $e_{s,g}$  being the sensible internal energy.  $Y_m$  is the mass fraction of  $m$ th species,  $D_g$  is the molecular diffusion coefficient, and  $D_g = \mu_g / (\rho_g Le)$ , where  $Le$  is the Lewis number (assumed to be unity in this work) and  $\mu_g$  is the dynamic viscosity.  $q_i$  is the  $i$ th component of the heat flux  $\mathbf{q} = -k_g \nabla T_g$ , with  $k_g$  being the gas thermal

conductivity and  $T_g$  being the gas temperature. In addition, the pressure is updated from the ideal gas equation of state,

$$p_g = \rho_g R_g T_g, \quad (5)$$

where  $R_g = R_0 / M_g$  is the specific gas constant, with  $R_0 = 8.314 \text{ J}/(\text{mol K})$  being the universal gas constant and  $M_g$  being the molecular weight of the gas.

The source terms,  $S_m$ ,  $S_{M,i}$ ,  $S_e$ , and  $S_{Y_m}$ , in Eqs. (1)–(4) denote the exchanges of mass, momentum, energy, and species between the gas and liquid phases. They are estimated as

$$S_m = -\frac{1}{V_c} \sum_1^{N_{dc}} \dot{m}_d, \quad (6)$$

$$S_{M,i} = -\frac{1}{V_c} \sum_1^{N_{dc}} (-\dot{m}_d u_{d,i} + F_{d,i} + F_{p,i}), \quad (7)$$

$$S_e = -\frac{1}{V_c} \sum_1^{N_{dc}} (\dot{Q}_c + \dot{Q}_{lat}), \quad (8)$$

$$S_{Y_m} = \begin{cases} S_m & \text{for the liquid species} \\ 0 & \text{for other species.} \end{cases} \quad (9)$$

Here,  $V_c$  is the volume of a CFD cell,  $N_{dc}$  is the droplet number in the cell,  $\dot{m}_d$  is the evaporation rate of a single droplet and is given later in Eq. (15), and  $u_{d,i}$  is the velocity component of the droplet in the  $i$ th direction.  $-\dot{m}_d u_{d,i}$  represents the rate of momentum transfer because of droplet evaporation, while  $F_{d,i}$  and  $F_{p,i}$  are the drag and PGF exerted on the droplet in the  $i$ th direction, respectively, and are given in Eqs. (24) and (26). For Eq. (7), other forces (e.g., gravity and Magnus lift force) are not considered in the present work. In Eq. (8),  $\dot{Q}_c$  is the convective heat transfer rate between the droplet and gas phases, while  $\dot{Q}_{lat}$  is the evaporation-induced heat transfer relating to latent heat of droplet vaporization.

### B. Governing equations for liquid droplet phase

The monodispersed liquid phase is modeled as a large number of spherical droplets tracked by using the Lagrangian method.<sup>14</sup> The interactions between droplets are neglected since dilute spray is studied in this work, in which the volume fraction of dispersed droplets is typically less than 0.1%.<sup>15</sup> The droplet breakup is not considered here since in our simulations, the droplet Weber number is generally less than 12. This is lower than the critical Weber number for the droplet breakup estimated by Tarnogrodzki.<sup>16</sup> The governing equations of mass, momentum, and energy for individual droplets take the following form:

$$\frac{dm_d}{dt} = \dot{m}_d, \quad (10)$$

$$\frac{du_{d,i}}{dt} = \frac{F_{d,i} + F_{p,i}}{m_d}, \quad (11)$$

$$c_{p,d} \frac{dT_d}{dt} = \frac{\dot{Q}_c + \dot{Q}_{lat}}{m_d}, \quad (12)$$

respectively, where  $m_d$  is the mass of a single droplet and can be calculated as  $m_d = \pi \rho_d d_d^3 / 6$  for spherical droplets, with  $\rho_d$  and  $d_d$  being

the droplet density and diameter, respectively.  $c_{p,d}$  is the droplet heat capacity, and  $T_d$  is the droplet temperature. Both  $\rho_d$  and  $c_{p,d}$  are functions of droplet temperature  $T_d$  to account for the thermal expansion when the droplet is heated,<sup>17</sup>

$$\rho_d(T_d) = \frac{a_1}{a_2^{1+(1-T_d/a_3)^{a_4}}}, \quad (13)$$

$$c_{p,d}(T_d) = b_1 + T_d \{ b_2 + T_d \{ b_3 + T_d [ b_4 + T_d ( b_5 + T_d b_6 ) ] \} \}, \quad (14)$$

where  $a_1, a_2, a_3, a_4$  and  $b_1, b_2, b_3, b_4, b_5, b_6$  are the species-specific constants.<sup>17</sup>

The evaporation rate,  $\dot{m}_d$ , in Eq. (10) is estimated through<sup>18</sup>

$$\dot{m}_d = -\pi \rho_s d_d Sh D_{ab} \ln(1 + B_M), \quad (15)$$

where  $\rho_s = p_s M_d / R_0 T_s$  is the vapor density at the droplet surface.  $p_s$  and  $T_s$  are the vapor pressure and temperature at the droplet surface, respectively,  $M_d$  is the molecular weight of the vapor.  $T_s$  is estimated using the two-third rule, i.e.,  $T_s = (2T_d + T_g)/3$ .<sup>18</sup> The Spalding mass transfer number,<sup>18</sup>  $B_M$ , is given as

$$B_M = \frac{Y_s - Y_g}{1 - Y_s}, \quad (16)$$

where  $Y_s$  and  $Y_g$  are the vapor mass fractions at the droplet surface and in the ambient gas phase, respectively.  $Y_s$  can be calculated as

$$Y_s = \frac{M_d X_s}{M_d X_s + M_{ed}(1 - X_s)}, \quad (17)$$

where  $M_{ed}$  is the averaged molecular weight of the mixture excluding the vapor at the droplet surface and  $X_s$  is the mole fraction of the vapor at the droplet surface, which is calculated using Raoult's law,

$$X_s = X_{liq} \frac{p_{sat}}{p_s}, \quad (18)$$

in which  $X_{liq}$  is the mole fraction of the liquid species in the liquid mixture.  $p_{sat}$  is the saturated vapor pressure and is estimated as a function of droplet temperature,<sup>17</sup>

$$p_{sat}(T_d) = p_g \cdot \exp\left(c_1 + \frac{c_2}{T_d} + c_3 \ln T_d + c_4 T_d^{c_5}\right), \quad (19)$$

where  $c_1, c_2, c_3, c_4$ , and  $c_5$  are constants.<sup>17</sup> Equation (19) is a modified version of the classical Clausius–Clapeyron equation, and it fits the data accurately even much above the normal boiling point.<sup>17</sup> Hence, it is expected to handle the droplet evaporation more accurately in shocked or reactive flows.<sup>19</sup> Similarly, the vapor pressure at the droplet surface  $p_s$  is a function of droplet surface temperature  $T_s$ , i.e.,

$$p_s(T_s) = X_{liq} p_g \cdot \exp\left(c_1 + \frac{c_2}{T_s} + c_3 \ln T_s + c_4 T_s^{c_5}\right). \quad (20)$$

The vapor mass diffusivity in the gaseous mixture in Eq. (15),  $D_{ab}$ , is modeled as<sup>20</sup>

$$D_{ab} = 10^{-3} \frac{T_s^{1.75}}{p_s} \sqrt{\frac{1}{M_d} + \frac{1}{M_g}} / \left( V_1^{1/3} + V_2^{1/3} \right)^2, \quad (21)$$

where  $V_1$  and  $V_2$  are constants.<sup>21</sup> Equation (21) has comparable accuracy to the classical Chapman–Enskog kinetic theory but is

more universal since the latter necessitates empirical parameters and simplifications.<sup>21</sup>

The Sherwood number in Eq. (15),  $Sh$ , is<sup>22</sup> given as

$$Sh = 2.0 + 0.6 Re_d^{1/2} Sc^{1/3}, \quad (22)$$

where  $Sc$  is the Schmidt number of the gas phase. The droplet Reynolds number in Eq. (22),  $Re_d$ , is defined based on the slip velocity between two phases, i.e.,

$$Re_d \equiv \frac{\rho_g d_d |u_{g,i} - u_{d,i}|}{\mu_g}. \quad (23)$$

The Stokes drag in Eq. (11),  $F_{d,i}$ , is modeled as (assuming that the droplet is spherical)<sup>23</sup>

$$F_{d,i} = \frac{1}{8} \pi d_d^2 \rho_g C_d |u_{g,i} - u_{d,i}| (u_{g,i} - u_{d,i}), \quad (24)$$

where  $C_d$  is the drag coefficient and is estimated as<sup>23</sup>

$$C_d = \begin{cases} \frac{24}{Re_d} \left( 1 + \frac{1}{6} Re_d^{2/3} \right), & Re_d \leq 1000, \\ 0.424, & Re_d > 1000. \end{cases} \quad (25)$$

It has been shown from the studies by Cheatham and Kailasanath<sup>24</sup> that the estimations in Eq. (25) can accurately predict the velocity distributions of shock-containing flow fields.

The pressure gradient force in Eq. (11),  $F_{p,i}$ , accounts for the strong local pressure variation at the rarefaction waves or shock discontinuities. It is given as

$$F_{p,i} = -\frac{1}{6} \pi d_d^3 \frac{\partial p_g}{\partial x_i}. \quad (26)$$

The convective heat transfer rate,  $\dot{Q}_c$ , in Eq. (12) is given as

$$\dot{Q}_c = h_c A_d (T_g - T_d), \quad (27)$$

where  $A_d = \pi d_d^2$  is the droplet surface area.  $h_c$  is the convective heat transfer coefficient calculated from the Nusselt number  $Nu$  using the Ranz and Marshall correlation,<sup>22</sup>

$$Nu = \frac{h_c d_d}{k_g} = 2.0 + 0.6 Re_d^{1/2} Pr^{1/3}, \quad (28)$$

where  $Pr = \mu_g \cdot c_{p,g} / k_g$  is the Prandtl number of the gas and  $c_{p,g}$  is the heat capacity at constant pressure.

The evaporation-induced heat transfer,  $\dot{Q}_{lat}$ , in Eq. (12) is given as

$$\dot{Q}_{lat} = -\dot{m}_d h_d(T_d), \quad (29)$$

where  $h_d(T_d)$  is the latent heat of vaporization (or specific enthalpy of vaporization) at the droplet temperature  $T_d$  and is approximated with<sup>25</sup>

$$h_d(T_d) = d_1 \cdot (1 - T_r)^{[(d_2 \cdot T_r + d_3) \cdot T_r + d_4] \cdot T_r + d_5}, \quad (30)$$

where  $d_1, d_2, d_3, d_4$ , and  $d_5$  are species-specific constants and  $T_r = T_d / T_{cr}$ , with  $T_{cr}$  being the critical temperature.

### C. Numerical method

The governing equations of gas and liquid phases are solved by using a two-phase multi-component compressible flow solver, *RYrhoCentralFoam*.<sup>26</sup> It is developed from a *rhoCentralFoam* solver in an OpenFOAM 5.0 package.<sup>27</sup> The cell-centered finite volume method is used to discretize the gas phase equations [Eqs. (1)–(4)]. An implicit second-order Crank–Nicolson scheme is used for temporal discretization. A second-order central differencing scheme<sup>28</sup> is applied for calculating diffusive fluxes, whereas the semi-discrete Kurganov, Noelle, and Petrova (KNP) scheme<sup>29</sup> with a minmod flux limiter<sup>30</sup> is used for convective fluxes. The Lagrangian equations for the droplet phase [Eqs. (10)–(12)] are integrated with a first-order Euler implicit method. The gas phase quantities at the droplet location, e.g.,  $p_g$  in Eq. (19),  $u_{g,i}$  and  $\mu_g$  in Eq. (23), are linearly interpolated from the gas phase results solved from Eqs. (1)–(5). The exchange terms in the gas and droplet equations are updated at each time step with two-way coupling of the two phases. The Courant–Friedrichs–Lewy (CFL) number of the gas phase equations is 0.02, which corresponds to the physical time step of about  $10^{-8}$  s.

The *rhoCentralFoam* solver has been validated by Greenshields *et al.*<sup>27</sup> and Zhang *et al.*<sup>31</sup> with various canonical tests, including Sod’s shock tube problem, forward-facing step, supersonic jet, and shock–vortex interaction. The results show that the KNP scheme can capture flow discontinuities (e.g., shocks and rarefaction waves) accurately. Furthermore, its accuracy in predicting multi-component gaseous flows has been validated in various reacting or non-reacting cases.<sup>32–34</sup> The *RYrhoCentralFoam* solver and the implementation of droplet submodels (e.g., droplet evaporation and multi-species diffusion) have been verified and validated with a series of benchmark cases against the analytical solution and/or experimental data in our recent work.<sup>19,35</sup>

### III. PHYSICAL PROBLEM

According to the experimental work of Hanson *et al.*,<sup>36</sup> with spatially uniform aerosols, the flow behind the shock is nominally one-dimensional. Hence, one-dimensional shock wave propagation in water droplet mists is considered in this work. The one-dimensional simplification is also widely used for particle<sup>12,37,38</sup> or droplet<sup>7,11,39</sup> laden flows with shock waves. Figure 1(a) shows the schematic of the one-dimensional computational domain (which is 4.2 m in length and starts at  $x = -0.2$  m) and the initial distribution of the water droplets. It should be noted that computational domains are treated as three-dimensional in *RYrhoCentralFoam*. For one-dimensional scenarios, the reduced directions (e.g.,  $y$ - and  $z$ -directions in this study) are discretized with one cell, and the “empty” condition is applied (hence, no numerical fluxes).<sup>35</sup> However, the lengths of the computational domain in these directions (0.2 mm for both the  $y$ - and  $z$ -directions in our simulations) are still relevant for two-phase flow simulations, to determine the droplet phase quantities (e.g., number density and volume fraction) and their effects on the gas phase [e.g., Eqs. (6)–(9)].

The carrier gas is an  $O_2/N_2$  mixture with the mass fractions of 0.233 and 0.767, respectively. The right propagating shock is initiated at  $x = -0.1$  m, with a high-pressure spot at  $x < -0.1$  m. In the pre-shock region ( $x > -0.1$  m), the initial gas temperature

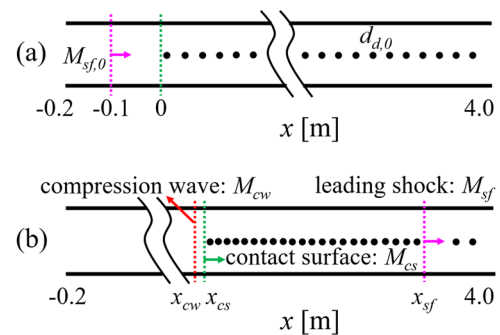


**FIG. 1.** Schematic of shock wave propagation in water droplet mists (a) before and (b) after the shock enters the two-phase region.  $M_{sf,0}$  is the Mach number of the incident shock initiated at  $x = -0.1$  m, and  $d_{d,0}$  is the initial diameter of water droplets.  $M_{sf}$ ,  $M_{cs}$ , and  $M_{cw}$  are the Mach numbers of leading shock, contact surface, and compression wave. Circles: water droplets.

and pressure are 275 K and 66 kPa, respectively. These conditions are chosen consistently with the study of Goossens *et al.*<sup>40</sup> and Kersey *et al.*<sup>7</sup> Different incident shock Mach numbers are investigated, i.e.,  $M_{sf,0} = 1.17$ – $1.9$ . The droplets are monodispersed and uniformly distributed in the region of  $x > 0$  (i.e., the two-phase section). The considered initial diameters and number densities are  $5 \mu\text{m}$ – $20 \mu\text{m}$  and  $2.5 \times 10^{11}/\text{m}^3$ – $2 \times 10^{12}/\text{m}^3$ , respectively. The initial density, heat capacity, and temperature of the water droplets are  $1000.9 \text{ kg/m}^3$ ,  $4222.4 \text{ J/kg/K}$ , and  $275 \text{ K}$ , respectively. Meanwhile, the water droplets are quiescent at  $t = 0$ . Figure 1(b) shows an instantaneous scenario after the shock propagates into the two-phase gas–droplet region. Three characteristic fronts are observable from our simulations, i.e., the leading shock, contact surface (interface of the purely gaseous and droplet-laden regions), and compression wave (interface of the expansion wave and shocked gas).

### IV. MESH SENSITIVITY ANALYSIS

The domain in Fig. 1 is discretized with three meshes of 4200, 14 000, and 42 000 cells. They correspond to uniform cell sizes of 1.0 mm, 0.3 mm, and 0.1 mm, termed meshes M1, M2, and M3, respectively. One droplet-laden case with a shock Mach number of  $M_{sf,0} = 1.5$  and an initial droplet diameter of  $d_{d,0} = 5 \mu\text{m}$  is selected for mesh sensitivity analysis, which are detailed in Table I.  $N_c$  is the number of CFD cells,  $\Delta_L$  is the uniform cell size, and  $N_{d,c,0}$  is the initial droplet number in the cell. Note that although the initial numbers of the droplet per CFD cell are different, the

**TABLE I.** Mesh sensitivity analysis.

Cases #	M1	M2	M3
$\Delta_L$ (mm)	1.0	0.3	0.1
$N_c$	4200	14 000	42 000
$N_{d,c,0}$	10	3	1
$N_{d,0}$ ( $/\text{m}^3$ )		$5 \times 10^{11}$	

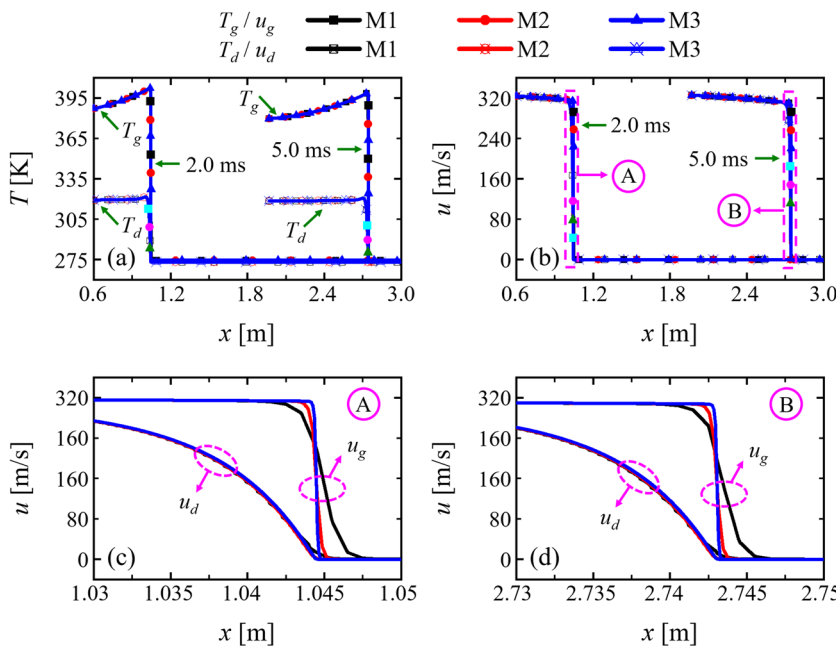


FIG. 2. Comparisons of (a) temperature and (b) velocity of gas and droplet phases with meshes M1, M2, and M3; (c) and (d) are enlarged views for A and B in Fig. 2(b).  $M_{sf,0} = 1.5$ ,  $d_{d,0} = 5 \mu\text{m}$ .

total number and the distributions of droplets in the entire domain are identical in the three cases, and the sensitivity of the statistical average in Eqs. (6)–(9) with respect to grid resolution will be studied.

Figure 2 shows the profiles of the temperature and velocity for both the carrier gas and droplets at  $t = 2.0$  ms and  $5.0$  ms for cases M1–M3. All the shown variables are from the Lagrangian results ( $T_g$  and  $u_g$  are interpolated to the droplet position). The near-shock regions [zones A and B in Fig. 2(b)] for  $t = 2.0$  ms and  $5.0$  ms are enlarged in Figs. 2(c) and 2(d). It is seen that the differences in the temperature and velocity of two phases ( $T_g$ ,  $T_d$ ,  $u_g$ , and  $u_d$ ) with different meshes are negligible. This is also true for other gas and droplet properties, e.g., gas viscosity, density, pressure, and droplet diameters. Closer inspection of the profiles at  $t = 2.0$  ms and  $5.0$  ms in Figs. 2(c) and 2(d) reveals that with coarser mesh resolution, the shock front gets slightly smoother. Nevertheless, all meshes accurately capture the shock front. Hence, both gas and droplet behaviors are not sensitive to the Eulerian mesh resolutions.

Figure 3 shows the profiles of exchange terms in mass, momentum, and energy equations [Eqs. (6)–(8)] for cases M1–M3. The numbers of droplets per cell (normalized by the corresponding  $N_{dc,0}$ ) are also shown. For  $S_m$ ,  $S_{M,i}$ , and  $S_e$ , the results from M3 have strong fluctuations in the regions between the leading shock and the contact surface, respectively, indicated by dashed lines C and D, although their averaged profiles are close with different meshes. Here, the average is based on the number of droplets per cell, i.e., divided by  $N_{dc}$ . The fluctuations of  $S_m$ ,  $S_{M,i}$ , and  $S_e$  are caused by the variations of  $N_{dc}$ . For finest mesh M3, droplet movement may cause a significant change in the droplet number in a cell. This is confirmed by  $N_{dc}$  distribution in Fig. 3(a), where the fluctuations in  $N_{dc}$  increase with mesh resolution. These findings are also true for other shock Mach numbers. Based on Figs. 2 and 3, further

decreasing the mesh resolution based on M1 would lead to a smoother shock front, whereas increasing it results in stronger fluctuations of interphase exchanges. Therefore, M1 is used for the following analyses.

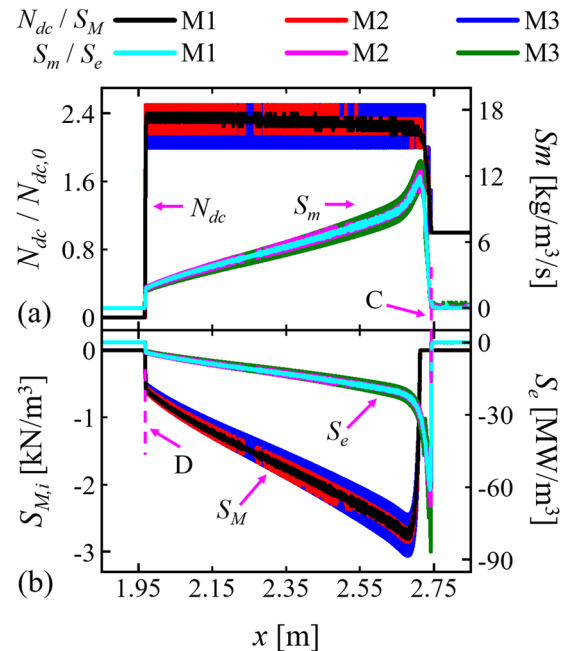


FIG. 3. Comparisons of the (a) number of droplets per cell and mass exchange term and (b) momentum and energy exchange terms with meshes M1, M2, and M3.  $M_{sf,0} = 1.5$ ,  $d_{d,0} = 5 \mu\text{m}$ .

V. RESULTS AND DISCUSSION

A. Effects of initial droplet diameter

The effects of the initial water droplet diameter are studied in this section. Four diameters are considered, i.e.,  $d_{d,0} = 5 \mu\text{m}$ ,  $10 \mu\text{m}$ ,  $15 \mu\text{m}$ , and  $20 \mu\text{m}$ . The shock Mach number and droplet number density are fixed to be  $M_{sf,0} = 1.17$  and  $N_{d,0} = 5 \times 10^{11}/\text{m}^3$ , respectively. The resulting initial droplet volume fractions are  $V_{fd,0} = 0.82 \times 10^{-5}$ ,  $6.55 \times 10^{-5}$ ,  $22.09 \times 10^{-5}$ , and  $52.36 \times 10^{-5}$ , respectively. Figures 4(a) and 4(b) show the profiles of the temperature and velocity for both gas and droplets at a representative instant, i.e.,  $t = 5 \text{ ms}$ . The results from the droplet-free case are also shown for comparison. It is seen that  $T_g$  is more significantly decreased in the post-shock region [i.e., behind the arrows in Fig. 4(a), which indicate the shock positions] with increased  $d_{d,0}$ . This is because larger droplets can absorb more heat from the gas phase, due to convective heat transfer and droplet evaporation. Note that the droplet equilibrium temperature near the two-phase contact surface is close for different cases, but it takes a longer time to reach the equilibrium value for larger  $d_{d,0}$ . The gradient of  $T_g$  near the leading shock also gets weaker with an increased droplet size, and the original shock degrades to a sonic wave when  $d_{d,0} = 20 \mu\text{m}$ . Note that there is a local increase in  $T_g$  in the locations marked by ellipse A in Fig. 4(a). This corresponds to the traveling compression wave between the expansion wave and shocked gas, which is originated from  $x = -0.1 \text{ m}$  at  $t = 0 \text{ s}$  [see Fig. 1(a)]. Therefore, higher (lower) total pressure and lower (higher) total temperature of this compressive wave can be observed, relative to its right (left) side. A similar increase in the gas temperature near the contact surface has also been observed by Kersey *et al.*<sup>7</sup> A more thorough examination of the wave structures in the flow field resulting from the interaction of a planar shock (two-dimensional) with a cloud of droplets has been performed by Chauvin *et al.*<sup>8</sup> In their work, more complex wave structures and wave-droplet interactions are caused by the end-walls of the shock tube facility, e.g., extra expansion waves from the driver end-wall and reflected shock or compression waves from the driven end-wall. However, basic

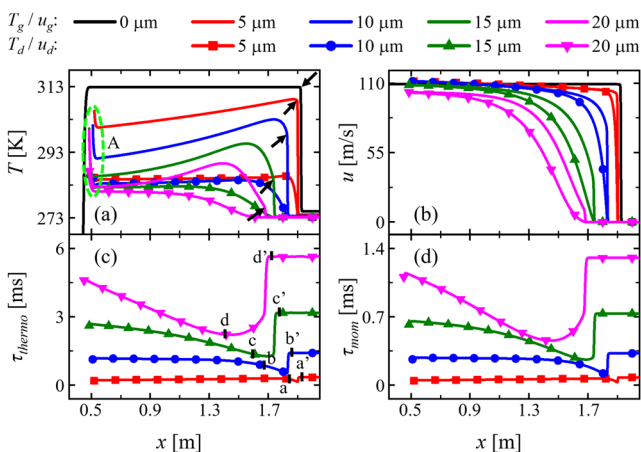


FIG. 4. Comparisons of the (a) temperature and (b) velocity for gas and droplet phases and (c) droplet thermal and (d) momentum response timescales at  $t = 5 \text{ ms}$  for different droplet diameters.

wave structures, including incident shock, compression wave, and contact surface, are similar to ours.

It is seen from Fig. 4(b) that the shock is little affected by small droplets (e.g.,  $5 \mu\text{m}$ ), due to the low volume fraction. For larger droplets (e.g.,  $20 \mu\text{m}$ ), even the equilibrium gas velocity  $u_{g,eq}$  (the final velocity at the two-phase contact surface) cannot be recovered to that of the droplet-free case. The velocity equilibrium also takes a longer distance with increased  $d_{d,0}$ . The gradient for the gas velocity at the shock front is considerably reduced, indicating the pronounced shock attenuation. This is confirmed by Fig. 5, which shows the evolutions of the instantaneous shock wave strength ( $S_{sf}$ , measured as the maximum magnitude of pressure gradient,  $|\nabla p_g|_{max}$ ) and Mach number ( $M_{sf}$ , calculated as the propagation velocity of the leading shock divided by the local speed of sound). It is seen from Fig. 5(a) that the strength of the propagating shock decreases in the droplet-laden gas, which is more remarkable for larger droplets. This can be confirmed by the consistently reduced shock Mach number. When  $d_{d,0} = 20 \mu\text{m}$ , the leading shock is reduced to an acoustic wave with  $M_{sf} \approx 1$  when  $x > 2.3 \text{ m}$ .

Figures 4(c) and 4(d) show the characteristic timescales for thermal and momentum responses for all the droplets at  $t = 5 \text{ ms}$ , respectively. For a droplet in saturated gas, there is no evaporation, and hence, only convective heat transfer proceeds. Based on Eqs. (12), (27), and (28), the droplet temperature equation is reduced to

$$c_{p,d} \frac{dT_d}{dt} = \frac{6Nu \cdot k_g}{\rho_d \cdot d_d^2} (T_g - T_d). \quad (31)$$

Integration of Eq. (31) yields the thermal response time,

$$\tau_{thermo} = \frac{c_{p,d} \cdot \rho_d \cdot d_d^2}{6Nu \cdot k_g}. \quad (32)$$

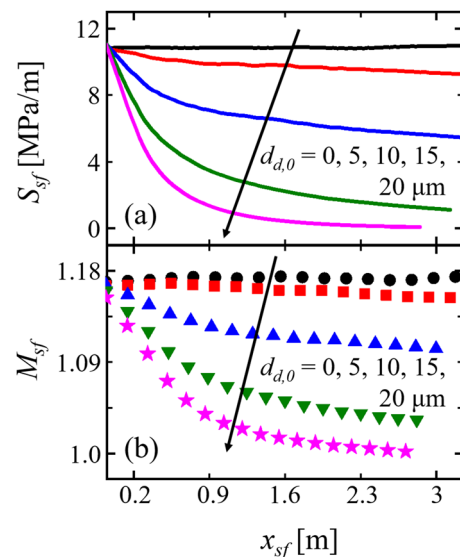


FIG. 5. Evolutions of the (a) shock strength and (b) Mach number.

For a droplet with  $Re_d \ll 1$ , based on Eqs. (11) and (24)–(26), the momentum response time is expressed as

$$\frac{1}{\tau_{mom}} = \frac{18\mu_g}{\rho_d \cdot d_d^2} - \frac{1}{\rho_d} \left( \frac{\partial p}{\partial x} \cdot \frac{1}{u_g - u_d} \right). \quad (33)$$

In Figs. 4(c) and 4(d), for the unperturbed droplets in front of the leading shock [i.e., before points a'–d' in Fig. 4(c)], their characteristic timescales are proportional to the square of diameters, as seen in Eqs. (32) and (33). Note that the pressure gradient is zero for these droplets. At the shock front, there is a sharp decrease in both  $\tau_{thermo}$  and  $\tau_{mom}$ , mainly due to the increased Nusselt number [ $Re_d$  increases; see Eq. (28)] and the pronounced PGF at the shock front, respectively. After then [e.g., after points a–d in Fig. 4(c)],  $\tau_{thermo}$  and  $\tau_{mom}$  increase and gradually level off with an increased off-shock distance. Hence, the effects of leading shock on the characteristic timescales only lie in a narrow region [e.g., a–a' for  $d_{d,0} = 5 \mu\text{m}$  in Fig. 4(c)], and the width of this region decreases with  $d_{d,0}$ . In some work,<sup>37,38,41,42</sup> such a region is termed “relaxation zone,” in which significant momentum and energy exchanges occur between the two phases until the equilibrium is reached. Furthermore,  $\tau_{thermo}$  is generally 4–6 times larger than  $\tau_{mom}$  for the same droplet in these cases, indicating that, for dispersed droplets, accommodation of the velocity to that of the continuous phase is generally much faster than that of temperature. This can be further confirmed in Figs. 7 and 9 later.

Figure 6 shows the evolutions of the droplet volume fraction in the  $x$ – $t$  diagram with four initial droplet diameters (5  $\mu\text{m}$ , 10  $\mu\text{m}$ , 15  $\mu\text{m}$ , and 20  $\mu\text{m}$ ). At the right side of lines A–D, the droplets are intact, and hence, the volume fractions are spatially uniform. Meanwhile, at the left side of lines A'–D', it is droplet-free, and the volume fraction is zero. It is interesting to find from Fig. 6(a) that the droplets of  $d_{d,0} = 5 \mu\text{m}$  can be quickly accelerated to the local gas speed due to their small momentum response times [see Fig. 4(d) and Eq. (33)]; the first term on RHS of Eq. (33) is large for small

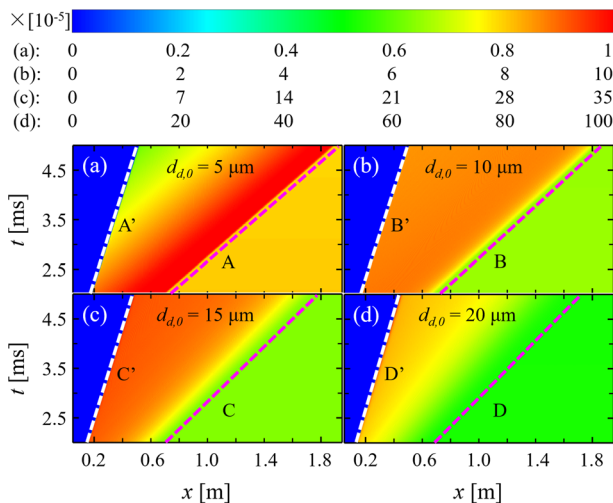


FIG. 6.  $x$ – $t$  diagram of the droplet volume fraction with droplet diameters of (a) 5  $\mu\text{m}$ , (b) 10  $\mu\text{m}$ , (c) 15  $\mu\text{m}$ , and (d) 20  $\mu\text{m}$ . A–D: leading shock; A'–D': contact surface.

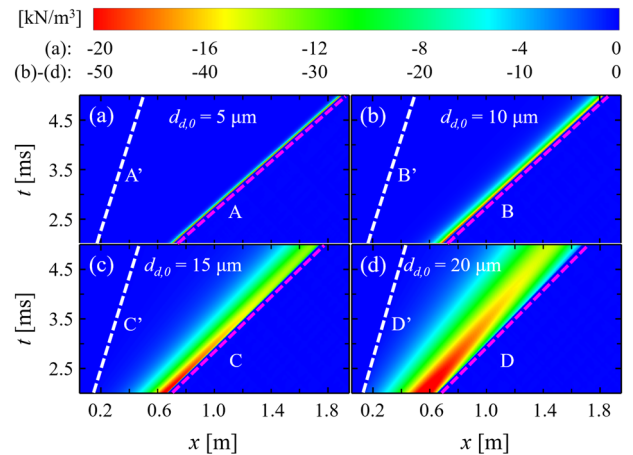
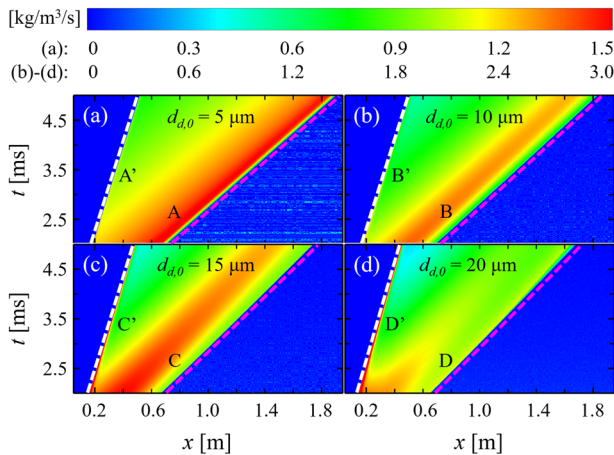


FIG. 7.  $x$ – $t$  diagram of the momentum exchange term with droplet diameters of (a) 5  $\mu\text{m}$ , (b) 10  $\mu\text{m}$ , (c) 15  $\mu\text{m}$ , and (d) 20  $\mu\text{m}$ . The description for dashed lines is the same as in Fig. 6.

$d_{d,0}$ , which hence makes the droplet volume fraction high immediately behind the leading shock. For  $d_{d,0} = 10 \mu\text{m}$  in Fig. 6(b), the droplets that freshly enter the shocked region have responded slowly to the local gas speed, due to the increased momentum response time [see Fig. 4(d)]. This leads to a transition distance with unchanged droplet volume behind the leading shock. However, further downstream, the volume fraction is almost uniform, which means that the droplets are propagating at the close velocities. For larger droplets ( $d_{d,0} = 15 \mu\text{m}$ ), the above transition distance is wider. This is more obvious when  $d_{d,0} = 20 \mu\text{m}$ , in which most of the droplets are accumulated at the contact surface [line D' in Fig. 6(d)].

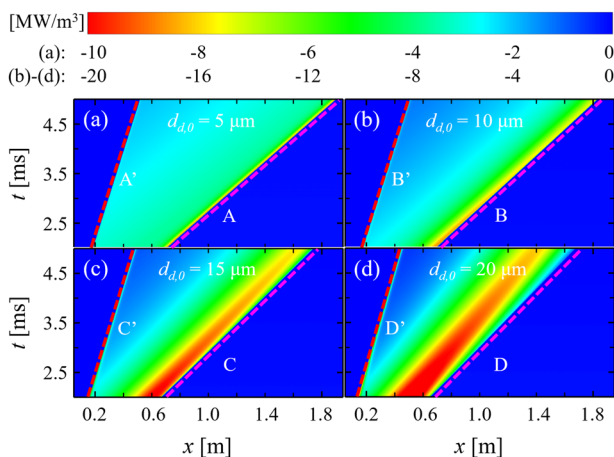
Figure 7 shows the evolutions of the momentum exchange term [ $S_{M,i}$  in Eq. (7)] for the gas phase in the  $x$ – $t$  diagram for the above-mentioned four cases. It is seen that interphase momentum exchange is completed immediately behind the leading shock when the initial droplet diameter is 5  $\mu\text{m}$ . Note that  $S_{M,i} \approx 0$  in the droplet-laden region means almost no interphase velocity difference, and hence, all droplets share the same speed to the gas. In addition, the momentum relaxation zone is narrow, and the width is almost constant with respect to time. However, this zone is extended for larger droplets (e.g., 10  $\mu\text{m}$ , 15  $\mu\text{m}$ , and 20  $\mu\text{m}$ ). This leads to almost uniform distribution of the droplet volume fraction after some distance of the leading shock in Fig. 6, especially for  $d_{d,0} = 5 \mu\text{m}$  and 10  $\mu\text{m}$ . In Figs. 7(c) and 7(d), the momentum relaxation becomes more distributed. One feature, different from that with small-sized droplets, is that the momentum exchange [particularly, the intensity, as shown in Figs. 7(c) and 7(d)] varies with time. This is caused by the evolving response of the droplets to the gradually weakened shock waves in these two cases, as indicated in Fig. 5.

Figure 8 shows the evolutions of the mass exchange term [i.e., volumetric evaporation rate,  $S_m$  in Eq. (6)] in the  $x$ – $t$  diagram when  $d_{d,0} = 5 \mu\text{m}$ , 10  $\mu\text{m}$ , 15  $\mu\text{m}$ , and 20  $\mu\text{m}$ . For  $d_{d,0} = 5 \mu\text{m}$ , strong evaporation occurs closely behind the leading shock and decreases gradually in the post-shock region. This is caused by the slow decrease in



**FIG. 8.**  $x-t$  diagram of the mass exchange term with droplet diameters of (a)  $5\ \mu\text{m}$ , (b)  $10\ \mu\text{m}$ , (c)  $15\ \mu\text{m}$ , and (d)  $20\ \mu\text{m}$ . The description for dashed lines is the same as in Fig. 6.

temperature after the leading shock [see Fig. 4(a)] and small interphase velocity difference [see Fig. 7(a)], which would result in moderate interphase heat transfer [shown in Fig. 9(a) later] for droplet evaporation. In the work of Watanabe *et al.*,<sup>43</sup> the front where evaporation first occurs behind the leading shock is termed evaporation front. It is also observable in our cases as significant evaporation generally lags behind the leading shock in Fig. 8. For  $d_{d,0} = 10\ \mu\text{m}$  and  $15\ \mu\text{m}$ , droplet evaporation becomes strong after a finite distance behind the leading shock. The distributions of the evaporation zones are almost constant with respect to time. For  $d_{d,0} = 20\ \mu\text{m}$ , within the shown period, droplet evaporation is considerably reduced, due to much lower gas temperature (see Fig. 4). The carrier gas cannot provide sufficient energy for droplet evaporation when the droplet volume fraction is sufficiently high.



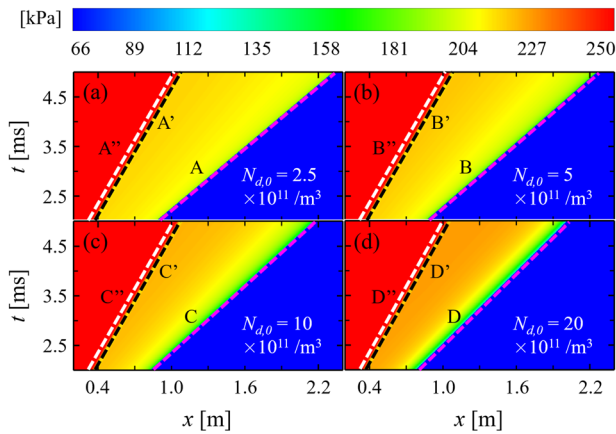
**FIG. 9.**  $x-t$  diagram of the energy exchange term with droplet diameters of (a)  $5\ \mu\text{m}$ , (b)  $10\ \mu\text{m}$ , (c)  $15\ \mu\text{m}$ , and (d)  $20\ \mu\text{m}$ . The description for dashed lines is the same as in Fig. 6.

Figure 9 shows the evolutions of the energy exchange term [ $S_e$  in Eq. (8)] in the  $x-t$  diagram. Generally, considerable energy transfer occurs earlier than the mass exchange when the shock wave sweeps. This is because droplet heating toward the saturated temperature occurs due to convective heat transfer, which takes a finitely long period. When the droplets reach the saturated temperature, significant evaporation can be observed. Therefore, with the same droplet size, the energy exchange zones with high  $|S_e|$  (e.g., above  $8\ \text{MW}/\text{m}^3$  for  $d_{d,0} = 5\ \mu\text{m}$  and  $16\ \text{MW}/\text{m}^3$  for  $d_{d,0} = 10\ \mu\text{m}$ ,  $15\ \mu\text{m}$ , and  $20\ \mu\text{m}$ ) are closer to the leading shock front than the droplet evaporation zone. Meanwhile, the energy exchange zone is remarkably narrower than the mass exchange zone for the droplets of  $d_{d,0} = 5\ \mu\text{m}$ ,  $10\ \mu\text{m}$ , and  $15\ \mu\text{m}$ . This implies that once the droplets are heated to high temperatures (relative to their initial temperature), they become self-sustainable and continuously evaporate with large  $S_m$  but with low  $|S_e|$ .

The spatial and temporal differences of interphase mass, momentum, and energy exchanges are worthy for further discussion. For fine water droplets (e.g.,  $5\ \mu\text{m}$ ), the timings for these exchanges are close. For large water droplets (e.g.,  $d_{d,0} = 10\ \mu\text{m}$  and  $15\ \mu\text{m}$ ), the difference between onsets of energy and momentum exchanges, as well as mass exchange, is more pronounced. This is because  $S_{M,i}$  mainly depends on the motions of gas and droplets. Note that the contribution to  $S_{M,i}$  from the first term (the momentum transfer from the evaporated vapor) on the RHS of Eq. (7) is small compared to the other two terms, as the volumetric evaporation rate  $S_m$  is generally four orders of magnitude smaller than that of  $|S_{M,i}|$  (see Figs. 7 and 8). However, variations of  $S_m$  and  $S_e$  depend on different local conditions, e.g., vapor saturability, interphase temperature difference, and droplet heating. This indicates that when the leading shock interacts with the droplets, the interphase momentum exchange is the major reason of shock attenuation, as considerable mass and energy exchanges lag remarkably farther behind the shock front. Hence, the shock attenuation is mainly affected by the instantaneous amount of droplets it interacts with.

### B. Effects of droplet number density

The effects of droplet number density on the propagating shock wave will be examined in this section. Figure 10 shows the evolutions of gas phase total pressure ( $p_{g,tot}$ ) in the  $x-t$  diagram with four different droplet number densities, i.e.,  $N_{d,0} = 2.5 \times 10^{11}/\text{m}^3$ ,  $5 \times 10^{11}/\text{m}^3$ ,  $1 \times 10^{12}/\text{m}^3$ , and  $2 \times 10^{12}/\text{m}^3$ . Their corresponding droplet volume fractions are  $3.27 \times 10^{-5}$ ,  $6.55 \times 10^{-5}$ ,  $13.09 \times 10^{-5}$ , and  $26.18 \times 10^{-5}$ , respectively. Here, the shock Mach number and the initial droplet diameter are  $M_{sf,0} = 1.35$  and  $d_{d,0} = 10\ \mu\text{m}$ , respectively. In Figs. 10(a)–10(d), the total pressure in the regions between lines  $A'$  and  $A''$ ,  $B'-B''$ ,  $C'-C''$ , and  $D'-D''$  (here,  $A'-D'$  denote the contact surfaces, and  $A''-D''$  denote the compression waves) is continuous to that behind lines  $A''-D''$ . This means that the contact surface, not the compression wave, is a jump interface for gas phase total pressure. In addition,  $p_{g,tot}$  monotonically increases in the droplet-laden areas, e.g., from  $A$  to  $A'$ . This is caused by the total pressure recovery from droplet evaporation, which acts as mass addition to the gas phase. Moreover, the larger droplet number density leads to stronger recovery, as can be seen from Figs. 10(a)–10(d). This can be further confirmed by the contours of  $Y_{\text{H}_2\text{O}}$  in Fig. 12. However, the total



**FIG. 10.**  $x-t$  diagram of gas total pressure with droplet number densities of (a)  $2.5 \times 10^{11}/\text{m}^3$ , (b)  $5 \times 10^{11}/\text{m}^3$ , (c)  $10 \times 10^{11}/\text{m}^3$ , and (d)  $20 \times 10^{11}/\text{m}^3$ . A–D: leading shock; A'–D': contact surface; A''–D'': compression wave.

pressure  $p_{g,tot}$  is relatively low immediately after the leading shock (lines A–D). This is caused by two factors, i.e., the shock-induced and droplet-induced (due to both drag and pressure gradient forces) gas pressure loss. Specifically, the initially quiescent droplets act as strong aerodynamic barriers to the incident shock. Furthermore, the droplet-induced pressure loss becomes stronger with increased  $N_{d,0}$ . This is because both drag and pressure gradient forces from droplets increase with droplet numbers that immediately interact with the shock front [see Eqs. (24) and (26), respectively]. Note that although pressure can be recovered to some extent due to droplet evaporation, however, it cannot reach the original value, i.e.,  $p_{g,tot}$  in the droplet-laden area is always lower than that of the driver gas (left to lines A''–D'').

Figure 11 shows the evolutions of gas phase total temperature ( $T_{g,tot}$ ) in the  $x-t$  diagram for the same cases as in Fig. 10. When the droplet number density is  $N_{d,0} = 2.5 \times 10^{11}/\text{m}^3$ ,  $T_{g,tot}$  varies slightly

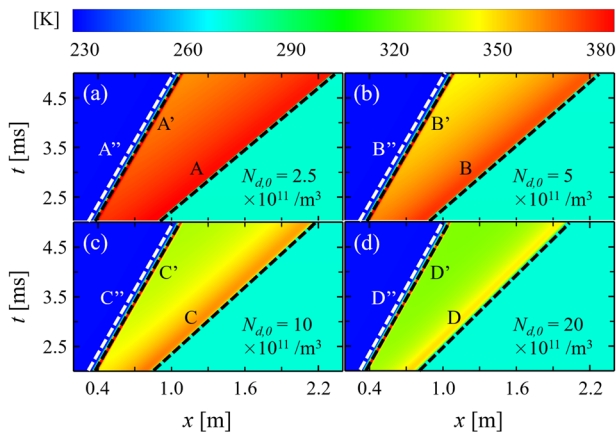
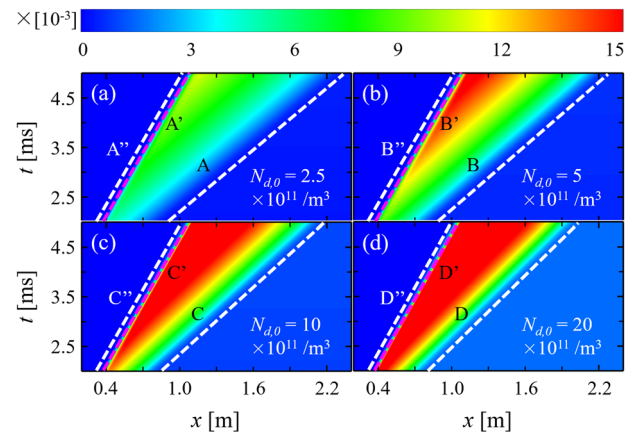


**FIG. 11.**  $x-t$  diagram of gas total temperature with droplet number densities of (a)  $2.5 \times 10^{11}/\text{m}^3$ , (b)  $5 \times 10^{11}/\text{m}^3$ , (c)  $10 \times 10^{11}/\text{m}^3$ , and (d)  $20 \times 10^{11}/\text{m}^3$ . The description for dashed lines is the same as in Fig. 10.

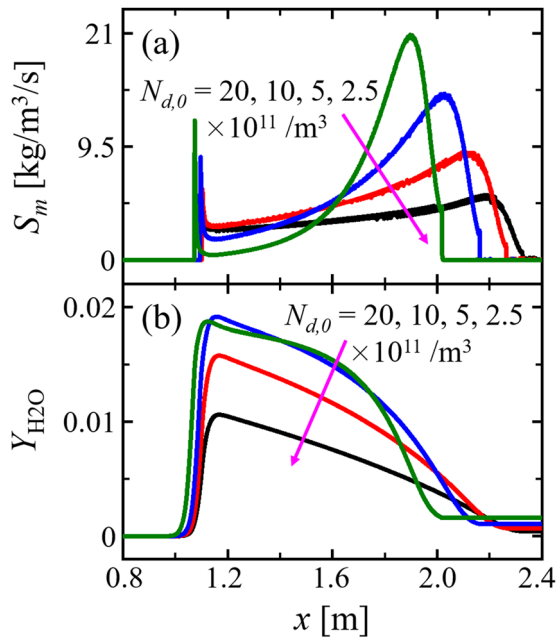
behind the leading shock (almost constant around 363 K). This is because of relatively weak heat exchange between the two phases. As  $N_{d,0}$  further increases,  $T_{g,tot}$  is considerably reduced due to heat transfer to the dispersed droplets. Meanwhile, with larger  $N_{d,0}$ , a more significant  $T_{g,tot}$  reduction is observable at the end of the post-shock evaporation zone. This would slow down droplet evaporation and interphase heat transfer. Furthermore,  $T_{g,tot}$  also decreases due to shock attenuation ( $Ma_g \downarrow$  is not shown here as already demonstrated in Fig. 5 and will be further confirmed in Fig. 14), droplet heat absorption ( $T_g \downarrow$ ), and vapor mass addition ( $\gamma_g \downarrow$ ) based on that  $T_{g,tot} = T_g \left( 1 + \frac{\gamma_g - 1}{2} Ma_g^2 \right)$ , with  $Ma_g$  and  $\gamma_g$  being the Mach number and the specific heat ratio of the carrier gas, respectively.

Figure 12 shows the evolutions of the  $\text{H}_2\text{O}$  mass fraction in the  $x-t$  diagram. Generally,  $Y_{\text{H}_2\text{O}}$  increases toward the contact surface, which is accumulated from continuous evaporation. For  $N_{d,0} = 2.5 \times 10^{11}/\text{m}^3$  and  $5 \times 10^{11}/\text{m}^3$ , the volumetric evaporation rate  $S_m$  [see Fig. 13(a), at  $t = 5.0$  ms, for example] is relatively low, whereas the gas is unsaturated even at  $t = 5.0$  ms [see Fig. 13(b)]. However, for  $N_{d,0} = 1 \times 10^{12}/\text{m}^3$  and  $2 \times 10^{12}/\text{m}^3$ , considerable vaporization (hence,  $S_m$ ) is found in the shocked gas, and water vapor concentration near the contact surface is high, as seen in Fig. 13. This is particularly true when  $N_{d,0} = 2 \times 10^{12}/\text{m}^3$  in Fig. 12(d), in which most of the area between D and D' is filled with  $\text{H}_2\text{O}$  vapor of high concentration. This can be confirmed by the shorter distance between where remarkable water concentration exists and the leading shock front (indicated by lines A–D in Fig. 12).

It is observed from Figs. 10–12 that the compression wave (A''–D'') is always on the left side of the contact surface (A'–D') that separates the two-phase region from the pure gas region, and therefore, the droplets cannot cross the compression waves. This is due to the following reasons. First, all the droplets have been accelerated to the local gas speed near the left end of the droplet-laden region (i.e., lines A'–D' in the  $x-t$  diagrams above). Hence, there is no slip velocity between the compression waves and the local droplets. Second, the compression wave results in a strong positive pressure gradient, which would act on and therefore accelerate the droplets if the droplets approach the compression wave.



**FIG. 12.**  $x-t$  diagram of the  $\text{H}_2\text{O}$  mass fraction with droplet number densities of (a)  $2.5 \times 10^{11}/\text{m}^3$ , (b)  $5 \times 10^{11}/\text{m}^3$ , (c)  $10 \times 10^{11}/\text{m}^3$ , and (d)  $20 \times 10^{11}/\text{m}^3$ . The description for dashed lines is the same as in Fig. 10.



**FIG. 13.** Comparisons of the (a) mass exchange term and (b) H<sub>2</sub>O mass fraction at  $t = 5$  ms for different droplet number densities.

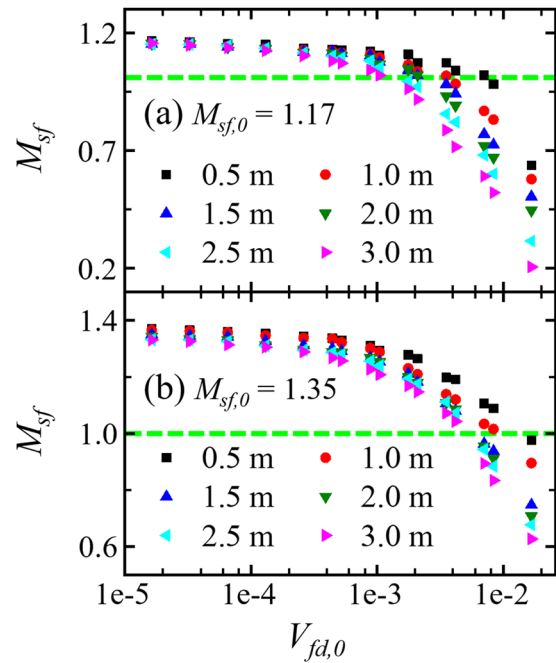


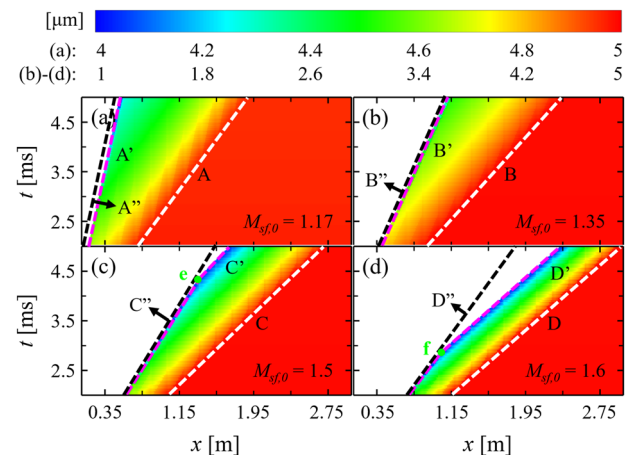
**FIG. 14.** Shock Mach numbers with various initial droplet volume fractions: (a)  $M_{sf,0} = 1.17$  and (b)  $M_{sf,0} = 1.35$ . Dashed lines: iso-lines of  $M_{sf} = 1.0$ .

The shock attenuation by the dispersed droplets is shown in Fig. 5. For a specific droplet volume fraction, the shock velocity is attenuated to the same value at the same location when it propagates downstream, regardless of the droplet size.<sup>39</sup> Figure 14 further studies this effect, through visualizing the shock Mach numbers at different streamwise locations, subject to various initial droplet volume fractions. For  $V_{fd,0} < 10^{-4}$ , the shocks are slightly attenuated when they propagate, as  $M_{sf}$  at different locations are quite close. Obvious shock attenuation occurs when  $V_{fd,0} > 10^{-4}$ . It is found from Fig. 14(a) that, with an initial Mach number of  $M_{sf,0} = 1.17$ ,  $M_{sf}$  quickly decays to less than 1.0 for  $x > 1.0$  m when  $V_{fd,0} > 4 \times 10^{-3}$ . For higher  $V_{fd,0}$  (e.g.,  $V_{fd,0} > 8 \times 10^{-3}$ ),  $M_{sf}$  is lower than 1.0 even before  $x = 0.5$  m. For  $M_{sf,0} = 1.35$  in Fig. 14(b),  $M_{sf} > 1$  for  $x = 0$  m–3.0 m when  $V_{fd,0} < 4 \times 10^{-3}$ . With further increased  $V_{fd,0}$ , the shocks finally evolve to pressure waves. Similar observation has been reported by Kersey *et al.*,<sup>7</sup> in which an incident shock with  $M_{sf,0} = 1.25$  is attenuated to a subsonic wave when the droplet mass loading is above 0.63. From Fig. 14, it is also seen that the shocks with higher  $M_{sf,0}$  can propagate farther downstream with larger  $V_{fd,0}$  before they are attenuated to sonic waves.

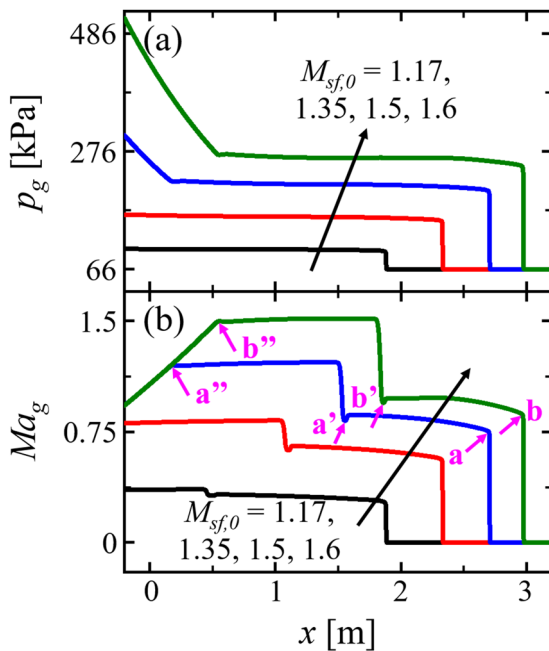
### C. Effects of incident shock Mach number

Figure 15 shows the evolutions of droplet diameters in the  $x$ - $t$  diagram with four incident shock Mach numbers, i.e.,  $M_{sf,0} = 1.17, 1.35, 1.5$ , and  $1.6$ . The corresponding initial compression wave Mach numbers are  $M_{cw,0} = 0.31, 0.61, 1.2$ , and  $1.5$ . Apparently, the compression wave is supersonic when  $M_{sf,0} = 1.5$  and  $1.6$ . The initial droplet diameter, number density, and volume fraction are

$d_{d,0} = 5 \mu\text{m}$ ,  $N_{d,0} = 1 \times 10^{12}/\text{m}^3$ , and  $V_{fd,0} = 1.64 \times 10^{-5}$ , respectively. Generally, in the shocked gas, the droplet diameter decreases continuously from the evaporation front. Near the leading shocks (lines A–D), the droplet diameter is about  $d_d = 4.95 \mu\text{m}$ , which is slightly smaller than  $d_{d,0} = 5 \mu\text{m}$  due to the slow evaporation in the quiescent air before the shock arrival. It is seen that  $d_d$  decreases faster with larger  $M_{sf,0}$  due to the increased interphase temperature difference. The smallest droplets are observed at the end of the



**FIG. 15.**  $x$ - $t$  diagram of droplet diameters with incident shock Mach numbers of (a) 1.17, (b) 1.35, (c) 1.5, and (d) 1.6. The description for dashed lines is the same as in Fig. 10.



**FIG. 16.** Distributions of the (a) pressure and (b) Mach number at  $t = 5.0$  ms for different incident shock Mach numbers. a/b: shock front; a'/b': compression wave; a''/b'': expansion wave.

two-phase region (lines A'–D'), due to their relatively larger residence time in the shocked gas and hence longer evaporation time. Note that the two-phase contact surfaces when  $M_{sf,0} = 1.5$  and  $1.6$ , i.e., C' and D', are demarcated with a turning point (i.e., e and f) into two sections [see Figs. 15(c) and 15(d)]. The probable reason for this phenomenon is that the contact surface (lines C' and D')

and compression wave (lines C'' and D'') behind the leading shock are supersonic in these two cases and is explained in detail below.

The recompression phenomenon can be justified from the distributions of static pressure  $p_g$  and Mach number  $Ma_g$ , which are shown in Fig. 16. The results are from a representative instant of  $t = 5$  ms. In Fig. 16(a) with  $M_{sf,0} = 1.5$  and  $1.6$ , it is seen that pressure behind the expansion wave [points a'' and b'' in Fig. 16(b)] is higher than that after the shock [points a and b in Fig. 16(b)] and compression [points a' and b' in Fig. 16(b)] waves. The higher pressure in the expansion wave accelerates the compression wave to catch up with the leading shock, which is decelerated by the droplets until the compression wave and shock wave reach a kinematic balance. After that, the leading shock and contact surface propagate at the same speed. This is why the leading shock is parallel to the contact surface in Figs. 15(c) and 15(d), after point e in  $M_{sf,0} = 1.5$  and point f in  $M_{sf,0} = 1.6$ , respectively. However, this phenomenon is not seen with lower incident Mach numbers (e.g.,  $M_{sf,0} = 1.17$  and  $1.35$ ). In Fig. 16(b), it is seen that the gas after the compression wave (but before the expansion wave) is supersonic in  $M_{sf,0} = 1.5$  and  $1.6$  but subsonic in  $M_{sf,0} = 1.17$  and  $1.35$ . Note that the recompression of the leading shock is only possible when the compression wave is supersonic. Although there is also acceleration of the compression wave to some extent when  $M_{sf,0} = 1.17$  and  $1.35$  (e.g., to  $0.36$  Ma and  $0.81$  Ma at  $t = 5$  ms, respectively), they do not reach supersonic propagation and hence have little effects on the leading shocks. Furthermore, the smaller the difference between  $M_{sf,0}$  and  $M_{cw,0}$  is, the faster the  $M_{sf}$  attenuates to  $M_{cw}$  (therefore, the earlier they balance), as seen in Fig. 15.

The interphase coupling behind the peculiar recompression process is further discussed in Figs. 17(a)–17(c), which show the evolutions of exchange terms for mass, momentum, and energy equations for the gas phase from the same cases in Figs. 15 and 16. The results are volume-integrated in the droplet-laden region. For  $M_{sf,0} = 1.17$  and  $1.35$ ,  $S_m$ ,  $S_{M,i}$ , and  $S_e$  change monotonically.

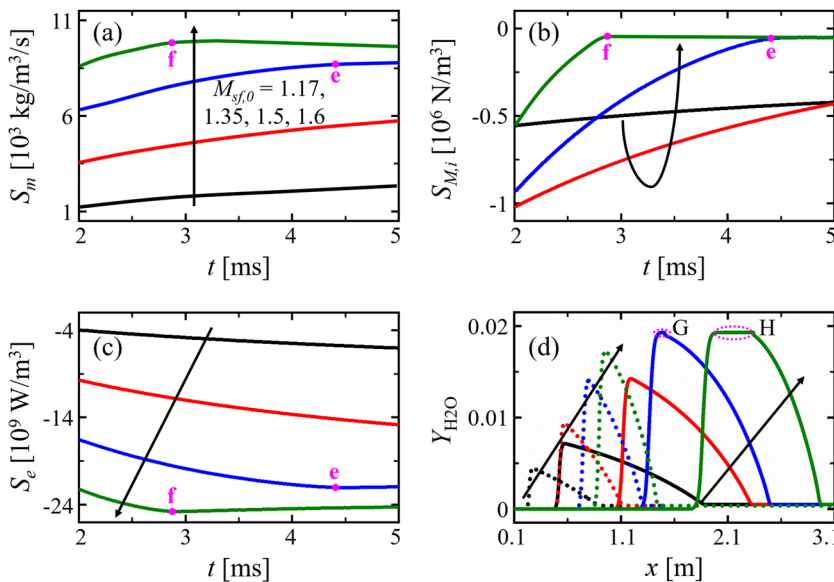


**FIG. 17.** Evolutions of volume-integrated (a) mass, (b) momentum, and (c) energy exchange rates in the droplet-laden region with various incident shock Mach numbers. (d) Profiles of the  $H_2O$  mass fraction at  $t = 2.5$  ms (dotted lines) and  $5.0$  ms (solid lines). Points e and f are the turning points in Fig. 15, and ellipses G and H are vapor-saturated regions.

However, for  $M_{sf,0} = 1.5$  and  $1.6$ , before their turning points (i.e., e and f in Fig. 17),  $S_m$ ,  $S_{M,i}$ , and  $S_e$  vary in similar tendency to those with lower shock Mach numbers. However, after the turning points, variations of  $S_m$ ,  $S_{M,i}$ , and  $S_e$  are limited. It is seen that  $S_m$  and  $|S_e|$  decrease slowly and almost linearly with time after the turning points, which indicates slightly weakened evaporation and heat transfer. This is because the region between the leading shock and the contact surface (i.e., the region between lines C and C' and D and D' in Fig. 15) approaches saturation [see the constant H<sub>2</sub>O vapor mass fraction of about 0.0193 at  $t = 5$  ms, circled by ellipses G and H in Fig. 17(d)] after the turning points. This is particularly true in the region close to the contact surface due to the higher shocked gas temperature, which develops faster to approach the saturation condition. Hence, the main contributions to  $S_m$  and  $S_e$  come from the droplets that just enter the shocked region. However, as the water droplets continuously enter, the gas velocity and temperature of this region slightly decrease with time, which then leads to a slow decrease in  $S_m$  and  $|S_e|$ . In addition, obvious momentum exchange only comes from the droplets that freshly enter the shocked region. The droplets well behind the shock have reached the kinematic equilibrium with the ambient gas. Hence,  $|S_{M,i}|$  is quite small as only the droplets close to the shock front have to be accelerated, and  $|S_{M,i}|$  almost decreases linearly and weakly due to the insignificant shock attenuation. From Figs. 15 and 17, it is found that for these two cases, the region between the leading shock and the contact surface reaches the steady state after the turning point, not only in terms of its structural width but also in terms of its two-phase interactions, e.g., mass, momentum, and energy exchange.

Based on the above analyses, it is found that whether the compression wave is supersonic is an indication of the recompression phenomenon. Figure 18 further shows the evolutions of the

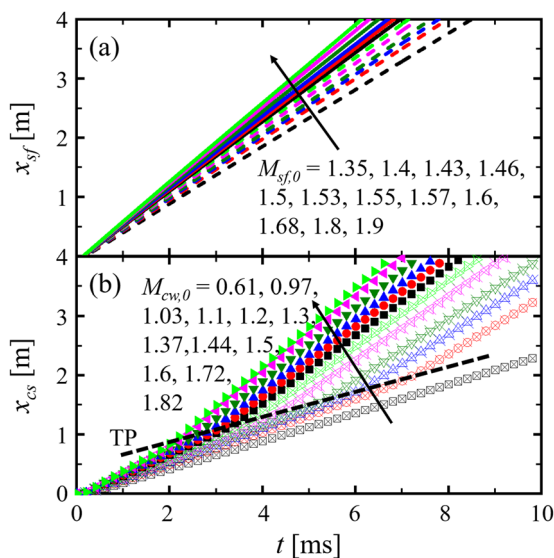


FIG. 18. Evolutions of (a) leading shock and (b) contact surface locations under various initial shock Mach numbers. The dashed line TP indicates the track of the turning points in different cases.

instantaneous locations of the leading shock ( $x_{sf}$ ) and contact surface ( $x_{cs}$ ) under various initial shock Mach numbers. All cases share identical the initial droplet diameter and number density in Figs. 15–17, i.e.,  $d_{d,0} = 5 \mu\text{m}$  and  $N_{d,0} = 1 \times 10^{12}/\text{m}^3$ . The initial leading shock and the corresponding compression wave Mach numbers are indicated in Figs. 18(a) and 18(b), respectively. It is seen that all cases with  $M_{cw,0} > 1.0$  can reach a balance between the leading shock and the two-phase contact surface, i.e., their velocities (slopes of their profiles) are almost the same after the turning points. Furthermore, the larger the  $M_{sf,0}$  is, the earlier the turning point occurs, and the closer the contact surface to the leading shock, which is confirmed in Figs. 15 and 17. Note that the case with  $M_{sf,0} = 1.4$  is slightly different, and the initial compression wave is subsonic ( $M_{cw,0} = 0.97$ ); however, the compression wave can be accelerated to be supersonic when the shock propagates. This acceleration is shown in Fig. 16 for cases  $M_{sf,0} = 1.17$  and  $1.35$ , mainly caused by the higher residual pressure in the left expansion wave than that in the compression wave when initiating the incident shock. For cases with  $M_{sf,0} \leq 1.35$ ,  $M_{cw}$  is subsonic throughout the computational domain although there is also acceleration of the compression wave (e.g.,  $M_{cw}$  from 0.61 initially to 0.81 at  $t = 5$  ms for  $M_{sf,0} = 1.35$ , as seen in Fig. 16), but there is no recompression phenomenon.

Finally, Fig. 19(a) shows evolutions of the distance between the leading wave and the two-phase contact surface under

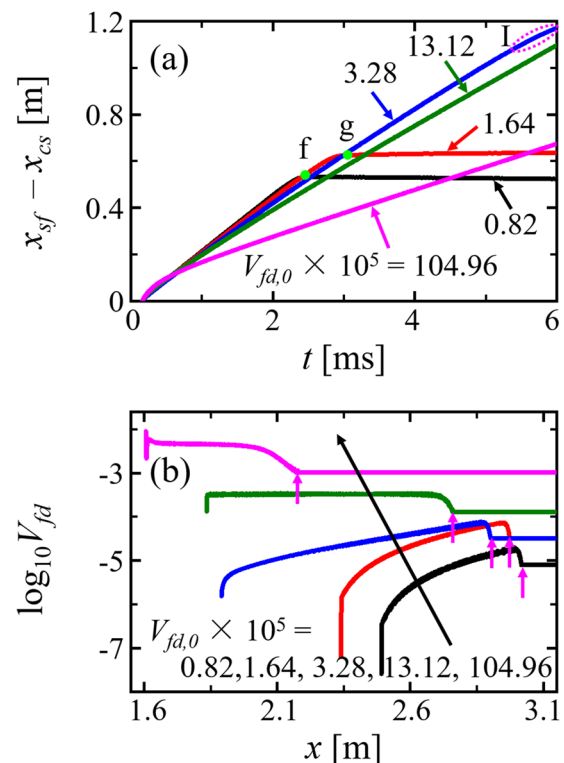


FIG. 19. Initial droplet volume fractions: (a) evolutions of the distance between the leading shock and the contact surface and (b) the droplet volume fraction (in logarithmic scale) at  $t = 5.0$  ms. The arrows in (b) indicate the instantaneous leading waves.

different droplet volume fractions. The incident shock Mach number is fixed to be 1.6. In Fig. 19(a), for  $V_{fd,0} = 0.82 \times 10^{-5}$  (the same case shown in Figs. 15–18 with  $M_{sf,0} = 1.6$ ) and  $1.64 \times 10^{-5}$ , recompression is observable after their respective turning points [f and g in Fig. 19(a)]. For  $V_{fd,0} = 3.28 \times 10^{-5}$ , recompression may occur after  $t \approx 5.5$  ms, as circled by ellipse I in Fig. 19(a). However, this weak recompression phenomenon is evolving (i.e.,  $x_{sf} - x_{cs}$  does not reach constant) even when the leading shock exits from the domain. For  $V_{fd,0} \geq 13.12 \times 10^{-5}$ , there is no recompression. Furthermore, the onset of the recompression phenomenon occurs later with a larger initial droplet volume fraction (no recompression may be regarded as the turning point at  $t \rightarrow +\infty$ ). Therefore, the initial droplet volume fraction also affects the occurrence of the recompression phenomenon.

Figure 19(b) shows the corresponding droplet volume fraction at  $t = 5.0$  ms. For  $V_{fd,0} = 0.82 \times 10^{-5}$  and  $1.64 \times 10^{-5}$ ,  $V_{fd}$  is low (e.g.,  $\leq 10^{-7}$ ) at the contact surface (i.e., the left end of each profile). Furthermore,  $V_{fd}$  decreases rapidly from its peak value after the leading shock [indicated by the arrow in Fig. 19(b)] to the contact surface. Therefore, attenuation of the supersonic compression wave behind the contact surface is weak based on Fig. 14, and recompression can occur. For  $V_{fd,0} = 3.28 \times 10^{-5}$ , it is seen that  $V_{fd} > 10^{-6}$  at the contact surface, and this condition is critical for the occurrence of the recompression process. For  $V_{fd,0} \geq 13.12 \times 10^{-5}$ ,  $V_{fd}$  gets higher at the contact surface, and recompression has no chance to occur. Based on Figs. 18 and 19, one can see that the recompression phenomenon is sensitive to the droplet volume fraction. For low  $V_{fd,0} = 0.82 \times 10^{-5}$ , recompression can occur even with a lower Mach number, e.g.,  $M_{sf,0} = 1.4$  and  $M_{cw,0} = 0.97$ . However, for a higher droplet volume fraction of  $V_{fd,0} = 3.28 \times 10^{-5}$ , it is difficult to occur even at  $M_{sf,0} = 1.6$  and  $M_{cw,0} = 1.5$ . Therefore, the condition for stable recompression is that the compression wave can be accelerated to the supersonic condition by the followed high-pressure expansion wave (see Fig. 16) but not attenuated excessively with high droplet loading.

## VI. CONCLUSION

The interactions between the propagating shock waves and dilute evaporating water droplets are investigated numerically in a one-dimensional domain. The exchanges in mass, momentum, energy, and vapor species between the carrier gas and droplets are considered through two-way coupling of the Eulerian–Lagrangian approach. Emphasis is laid on shock attenuation, two-phase interactions, droplet evaporation, motion, and heating dynamics. A parametric study is performed for the initial droplet diameters of  $5 \mu\text{m}$ – $20 \mu\text{m}$ , initial droplet number densities of  $2.5 \times 10^{11}/\text{m}^3$ – $2 \times 10^{12}/\text{m}^3$ , and incident shock Mach numbers of 1.17–1.9. Three characteristic fronts are observed when the shock travels in the two-phase gas–droplet medium: the leading shock that propagates right with the fastest velocity, the contact surface that separates the droplet-laden region from the droplet-free region, and the compression wave that follows behind the contact surface.

The variation of shock Mach numbers with droplet volume fractions indicates that remarkable shock attenuation takes place

when the initial droplet volume fraction is relatively large. For example, the propagating shock may be attenuated to sonic or even subsonic pressure waves when the initial droplet volume fractions are larger than  $10^{-3}$  and  $6 \times 10^{-3}$  for incident shock Mach numbers of 1.17 and 1.35, respectively. The attenuation is mainly caused by the momentum loss to those droplets that interact with the shock front and, hence, only depends on the instantaneous amount of shocked droplets (e.g., volume fraction or mass loading). Furthermore, shock compression, drag force, and pressure gradient force lead to remarkable total pressure loss immediately after the shock wave.

Moreover, the interphase heat transfer and evaporation effects of evaporative water droplets also play an important role in the post-shock region. The heat transfer to droplets decreases the shocked gas temperature. Droplet evaporation results in an increased water vapor concentration in the shocked gas, which dilutes the local mixtures behind the shock wave. Furthermore, this also contributes to the total pressure recovery behind the shock wave.

Gas recompression between the leading shock and the contact surface is found for high incident shock Mach numbers, which is because the attenuated leading shock reaches a balance with the following supersonic compression wave. When the recompression phenomenon occurs, the width of this recompressed region tends to be constant as the velocities of the leading shock (attenuated due to interactions with droplets) and compression wave (accelerated due to the residual of the high initial pressure for initiating the incident shock) are the same. Furthermore, the total amount of interphase exchanges in mass, momentum, and energy in this region also tends to be steady. The turning point in the  $x$ – $t$  diagram, after which the recompression phenomenon stabilizes, occurs earlier with an increased incident shock Mach number. For an initial droplet volume fraction of  $1.64 \times 10^{-5}$ , the recompression phenomenon always occurs when the incident shock Mach number is larger than 1.4. However, it is sensitive to the droplet volume fraction. For an incident shock Mach number of 1.6, recompression can only occur with initial droplet volume fractions below  $3.28 \times 10^{-5}$ .

A secondary breakup may be observed subject to incident shock waves, which may modulate the two-phase interactions, e.g., momentum and energy exchanges, because of the increased specific droplet surface area. Moreover, two- or three-dimensional simulations may be performed to further study the interaction between water droplets and incident shock waves. These are the interesting topics for our future studies.

## ACKNOWLEDGMENTS

The computational work for this article was fully performed through resources of the National Supercomputing Center, Singapore (<https://www.nscg.sg/>). This work was supported by the Singapore Ministry of Education Tier 1 (Grant No. R-265-000-688-114).

## DATA AVAILABILITY

The data that support the findings of this study are available from the corresponding author upon reasonable request.

## REFERENCES

- <sup>1</sup>W. Lu, W. Fan, K. Wang, Q. Zhang, and Y. Chi, "Operation of a liquid-fueled and valveless pulse detonation rocket engine at high frequency," *Proc. Combust. Inst.* **36**, 2657–2664 (2017).
- <sup>2</sup>S. M. Frolov, V. S. Aksenov, V. S. Ivanov, and I. O. Shamshin, "Continuous detonation combustion of ternary 'hydrogen–liquid propane–air' mixture in annular combustor," *Int. J. Hydrogen Energy* **42**, 16808–16820 (2017).
- <sup>3</sup>H. Watanabe, A. Matsuo, A. Chinnayya, K. Matsuoka, A. Kawasaki, and J. Kasahara, "Numerical analysis of the mean structure of gaseous detonation with dilute water spray," *J. Fluid Mech.* **887**, A4 (2020).
- <sup>4</sup>D. R. Haylett, P. P. Lappas, D. F. Davidson, and R. K. Hanson, "Application of an aerosol shock tube to the measurement of diesel ignition delay times," *Proc. Combust. Inst.* **32**, 477–484 (2009).
- <sup>5</sup>J. Santner and S. S. Goldsborough, "Hot-spot induced mild ignition: Numerical simulation and scaling analysis," *Combust. Flame* **209**, 41–62 (2019).
- <sup>6</sup>Y. Haruki, A. L. Pillai, T. Kitano, and R. Kurose, "Numerical investigation of flame propagation in fuel droplet arrays," *Atomization Sprays* **28**, 357–388 (2018).
- <sup>7</sup>J. Kersey, E. Loth, and D. Lankford, "Effect of evaporating droplets on shock waves," *AIAA J.* **48**, 1975–1986 (2010).
- <sup>8</sup>A. Chauvin, G. Jourdan, E. Daniel, L. Houas, and R. Tosello, "Experimental investigation of the propagation of a planar shock wave through a two-phase gas-liquid medium," *Phys. Fluids* **23**, 113301 (2011).
- <sup>9</sup>Y. Liang, Y. Jiang, C.-Y. Wen, and Y. Liu, "Interaction of a planar shock wave and a water droplet embedded with a vapour cavity," *J. Fluid Mech.* **885**, R6 (2020).
- <sup>10</sup>A. Kobiera, J. Szymczyk, P. Wolański, and A. Kuhl, "Study of the shock-induced acceleration of hexane droplets," *Shock Waves* **18**, 475–485 (2009).
- <sup>11</sup>G. Jourdan, L. Biamino, C. Mariani, C. Blanchot, E. Daniel, J. Massoni, L. Houas, R. Tosello, and D. Praguine, "Attenuation of a shock wave passing through a cloud of water droplets," *Shock Waves* **20**, 285–296 (2010).
- <sup>12</sup>G. Gai, O. Thomine, A. Hadjadj, and S. Kudriakov, "Modeling of particle cloud dispersion in compressible gas flows with shock waves," *Phys. Fluids* **32**, 023301 (2020).
- <sup>13</sup>W. A. Sirignano, *Fluid Dynamics and Transport of Droplets and Sprays*, 2nd ed. (Cambridge University Press, Cambridge, 2010), pp. 409–414.
- <sup>14</sup>G. B. Macpherson, N. Nordin, and H. G. Weller, "Particle tracking in unstructured, arbitrary polyhedral meshes for use in CFD and molecular dynamics," *Commun. Numer. Methods Eng.* **25**, 263–273 (2009).
- <sup>15</sup>C. T. Crowe, J. D. Schwarzkopf, M. Sommerfeld, and Y. Tsuji, *Multiphase Flows with Droplets and Particles* (CRC Press, 1998).
- <sup>16</sup>A. Tarnogrodzki, "Theoretical prediction of the critical weber number," *Int. J. Multiphase Flow* **19**, 329–336 (1993).
- <sup>17</sup>R. H. Perry, D. W. Green, and J. O. Maloney, *Perry's Chemical Engineers' Handbook*, 7th ed. (Choice Reviews Online, 1998).
- <sup>18</sup>B. Abramzon and W. A. Sirignano, "Droplet vaporization model for spray combustion calculations," *Int. J. Heat Mass Transfer* **32**, 1605–1618 (1989).
- <sup>19</sup>Z. Huang, M. Zhao, and H. Zhang, "Modelling *n*-heptane dilute spray flames in a model supersonic combustor fueled by hydrogen," *Fuel* **264**, 116809 (2020).
- <sup>20</sup>E. N. Fuller, P. D. Schettler, and J. C. Giddings, "New method for prediction of binary gas-phase diffusion coefficients," *Ind. Eng. Chem.* **58**, 18–27 (1966).
- <sup>21</sup>E. L. Cussler, *Diffusion: Mass Transfer in Fluid Systems*, 3rd ed. (Cambridge University Press, 2009).
- <sup>22</sup>W. E. Ranz and W. R. Marshall, "Evaporation from drops—Part I," *Chem. Eng. Prog.* **48**, 141–146 (1952).
- <sup>23</sup>A. B. Liu, D. Mather, and R. D. Reitz, "Modeling the effects of drop drag and breakup on fuel sprays," SAE Technical Paper No. 930072, 2010.
- <sup>24</sup>S. Cheatham and K. Kailasanath, "Numerical modelling of liquid-fuelled detonations in tubes," *Combust. Theory Modell.* **9**, 23–48 (2005).
- <sup>25</sup>B. E. Poling, J. M. Prausnitz, and J. P. O'Connell, *The Properties of Gases and Liquids*, 5th ed. (McGraw-Hill, New York, 2000).
- <sup>26</sup>See <https://Blog.Nus.Edu.Sg/Huangwei/Nus-Ryrhocentralfoam-Solver/> for more information about the development and validation of the RYrhoCentralFoam solver.
- <sup>27</sup>C. J. Greenshields, H. G. Weller, L. Gasparini, and J. M. Reese, "Implementation of semi-discrete, non-staggered central schemes in a colocated, polyhedral, finite volume framework, for high-speed viscous flows," *Int. J. Numer. Methods Fluids* **63**, 1–21 (2010).
- <sup>28</sup>H. Jasak, "Error analysis and estimation for the finite volume method with applications to fluid flows," Ph.D. thesis, Imperial College London, 1996.
- <sup>29</sup>A. Kurganov, S. Noelle, and G. Petrova, "Semidiscrete central-upwind schemes for hyperbolic conservation laws and Hamilton–Jacobi equations," *SIAM J. Sci. Comput.* **23**, 707–740 (2001).
- <sup>30</sup>P. L. Roe, "Characteristic-based schemes for the Euler equations," *Annu. Rev. Fluid Mech.* **18**, 337–365 (1986).
- <sup>31</sup>H. Zhang, M. Zhao, and Z. Huang, "Large eddy simulation of turbulent supersonic hydrogen flames with OpenFOAM," *Fuel* **282**, 118812 (2020).
- <sup>32</sup>Z. Huang and H. Zhang, "Numerical investigations of mixed supersonic and subsonic combustion modes in a model combustor," *Int. J. Hydrogen Energy* **45**, 1045–1060 (2020).
- <sup>33</sup>Z. Huang and H. Zhang, "Investigations of autoignition and propagation of supersonic ethylene flames stabilized by a cavity," *Appl. Energy* **265**, 114795 (2020).
- <sup>34</sup>M. Zhao, J.-M. Li, C. J. Teo, B. C. Khoo, and H. Zhang, "Effects of variable total pressures on instability and extinction of rotating detonation combustion," *Flow Turbul. Combust.* **104**, 261–290 (2020).
- <sup>35</sup>Z. Huang, M. Zhao, Y. Xu, G. Li, and H. Zhang, "Eulerian-Lagrangian modelling of detonative combustion in two-phase gas-droplet mixtures with OpenFOAM: Validations and verifications," *Fuel* **286**, 119402 (2021).
- <sup>36</sup>T. C. Hanson, D. F. Davidson, and R. K. Hanson, "Shock-induced behavior in micron-sized water aerosols," *Phys. Fluids* **19**, 056104 (2007).
- <sup>37</sup>C. T. Crowe, "Review—Numerical models for dilute gas-particle flows," *J. Fluids Eng.* **104**, 297–303 (1982).
- <sup>38</sup>O. Igra and G. Ben-Dor, "Dusty shock waves," *Appl. Mech. Rev.* **41**, 379–437 (1988).
- <sup>39</sup>E. J. Chang and K. Kailasanath, "Shock wave interactions with particles and liquid fuel droplets," *Shock Waves* **12**, 333–341 (2003).
- <sup>40</sup>H. W. J. Goossens, J. W. Cleijne, H. J. Smolders, and M. E. H. van Dongen, "Shock wave induced evaporation of water droplets in a gas-droplet mixture," *Exp. Fluids* **6**, 561–568 (1988).
- <sup>41</sup>H. J. Smolders and M. E. H. van Dongen, "Shock wave structure in a mixture of gas, vapour and droplets," *Shock Waves* **2**, 255–267 (1992).
- <sup>42</sup>G.-S. Yeom and K.-S. Chang, "Shock wave diffraction about a wedge in a gas-microdroplet mixture," *Int. J. Heat Mass Transfer* **53**, 5073–5088 (2010).
- <sup>43</sup>H. Watanabe, A. Matsuo, K. Matsuoka, A. Kawasaki, and J. Kasahara, "Numerical investigation on propagation behavior of gaseous detonation in water spray," *Proc. Combust. Inst.* **37**, 3617–3626 (2019).